Electronic Supplementary Material (ESI) for Physical Chemistry Chemical Physics.

High-Resolution Broadband Sum Frequency Generation Vibrational Spectroscopy Using Intrapulse Interference

*Yang Wang[1], Xiangyun Ma[1], Huijie Wang[1], Da Chen[1], Keng C. Chou[2], Qifeng Li[*1]*

1. School of Precision Instrument and Opto-electronics Engineering, Tianjin University, Tianjin, China.

2. Department of Chemistry, University of British Columbia, Vancouver, BC V6T 1Z1, Canada.

Corresponding Author

*E-mail: qfli@tju.edu.cn

Contents

1. The second-order nonlinear susceptibility

In sum frequency generation, the time-domain second-order nonlinear susceptibility can be expressed as[1-3]:

$$\chi^{(2)}(t) = A_{NR}\exp\left(i\psi_{NR}\right)\delta(t) - i\varepsilon(t)\sum_q A_q exp(- i\omega_q t)exp(- t/\tau_q) \tag{S1}$$

where A_{NR} and ψ_{NR} are the time-domain amplitude and the phase of the non-resonant background, respectively. A_q, ω_q and τ_q are amplitude, frequency, and dephasing time of the q[th] vibrational mode. $\delta(t)$ and $\varepsilon(t)$ represent the δ-function and Heaviside step function, respectively. The corresponding frequency-domain second-order nonlinear susceptibility $\chi(\omega)$ can be generated by Fourier transform from $\chi(t)$:[1, 4]

$$\chi^{(2)}(\omega) = A_{NR}\exp\left(i\Psi_{NR}\right) + \sum_q \frac{A_q}{\omega - \omega_q + i\Gamma_q} \tag{S2}$$

where Γ_q is the Lorentzian linewidth of the q[th] vibrational mode, $\Gamma_q = 1/(2\pi c\tau_q)$, and c is the speed of light.

2. The overview of the intrapulse interference SFG method

In the intrapulse interference SFG (II-SFG), we use the visible pulse $E_{vis}(t;\tau)$ as the gate pulse to probe the first-order polarization $P^{(1)}(t)$ by mapping the $I_{SFG}(\omega;\tau)$ with a series of time-delay τ. The overview of the II-SFG method is shown in Figure S1, which presents an iteration numerical processing. The $P^{(1)}_{out}(t)$ can be retrieved while the solution converges. The frequency-domain expression $P^{(1)}_{out}(\omega_{IR})$ is the Fourier transform of the time-domain $P^{(1)}_{out}(t)$. The $P^{(1)}(\omega_{IR})$ can be expressed as,

$$P^{(1)}(\omega_{IR}) = \chi^{(2)}(\omega_{SF})E_{IR}(\omega_{IR}) \tag{S3}$$

The complex frequency-domain second-order nonlinear susceptibility $\chi^{(2)}(\omega)\ can\ be\ obtained$ with $P^{(1)}_{out}(\omega_{IR})$ divided by $E_{IR}(\omega_{IR})$.

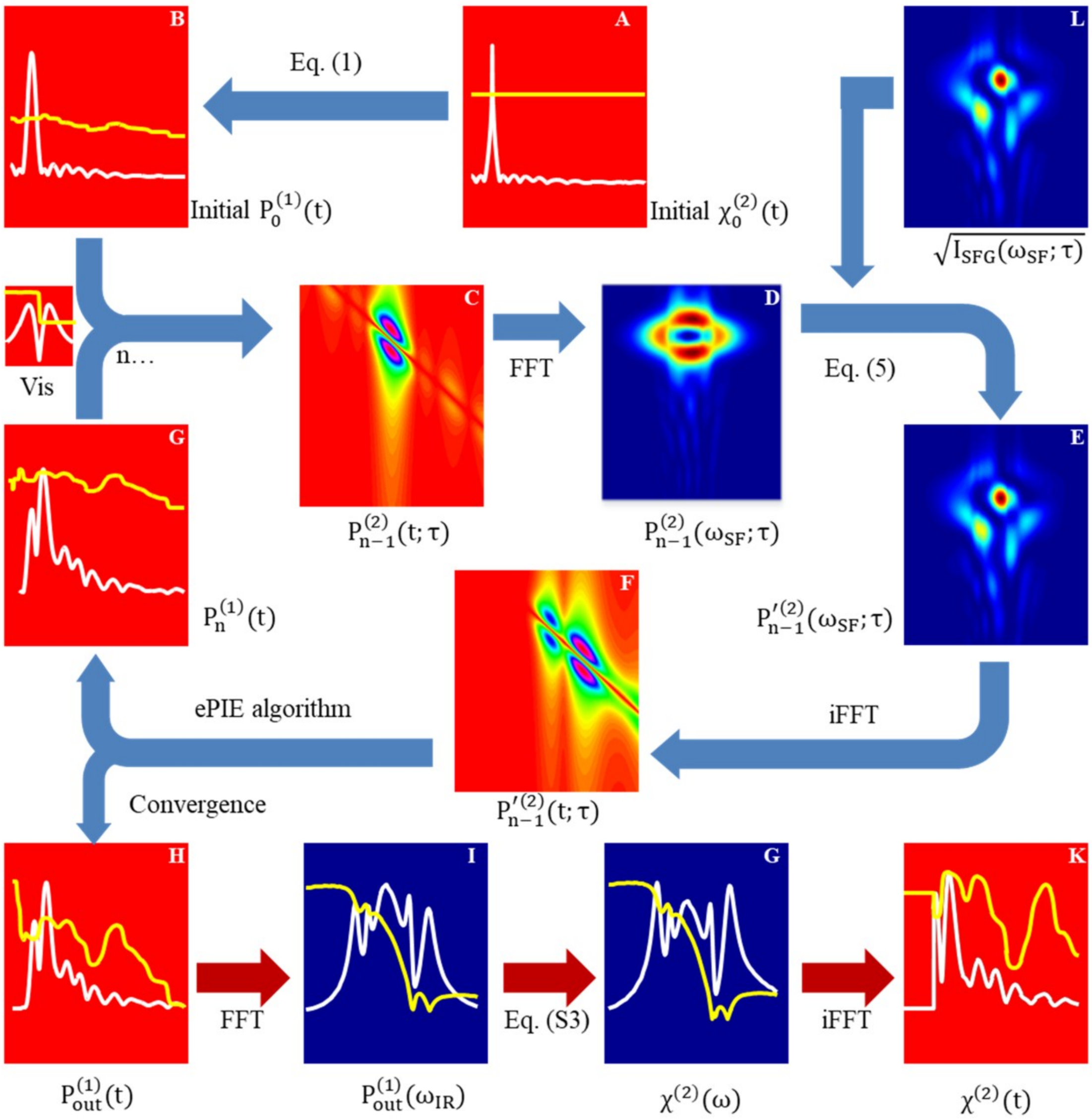

Figure S1. The overview of the II-SFG method.

3. The resolution of the II-SFG method

We have verified the resolution of the II-SFG by using a virtual second-order nonlinear susceptibility, the parameters is shown in Table S1.

Table S1. The parameters of the virtual second-order nonlinear susceptibility.

mode	ω (cm^{-1})	Γ (cm^{-1})	A
1	2945	2	1
2	2965	2	1
A_{NR}		0.05	

As shown in Figure S2, when the linewidth of the $\chi^{(2)}(\omega)$ is narrow enough, Γ=2 cm^{-1}. The resolution of the II-SFG is the resolution of the spectrometer.

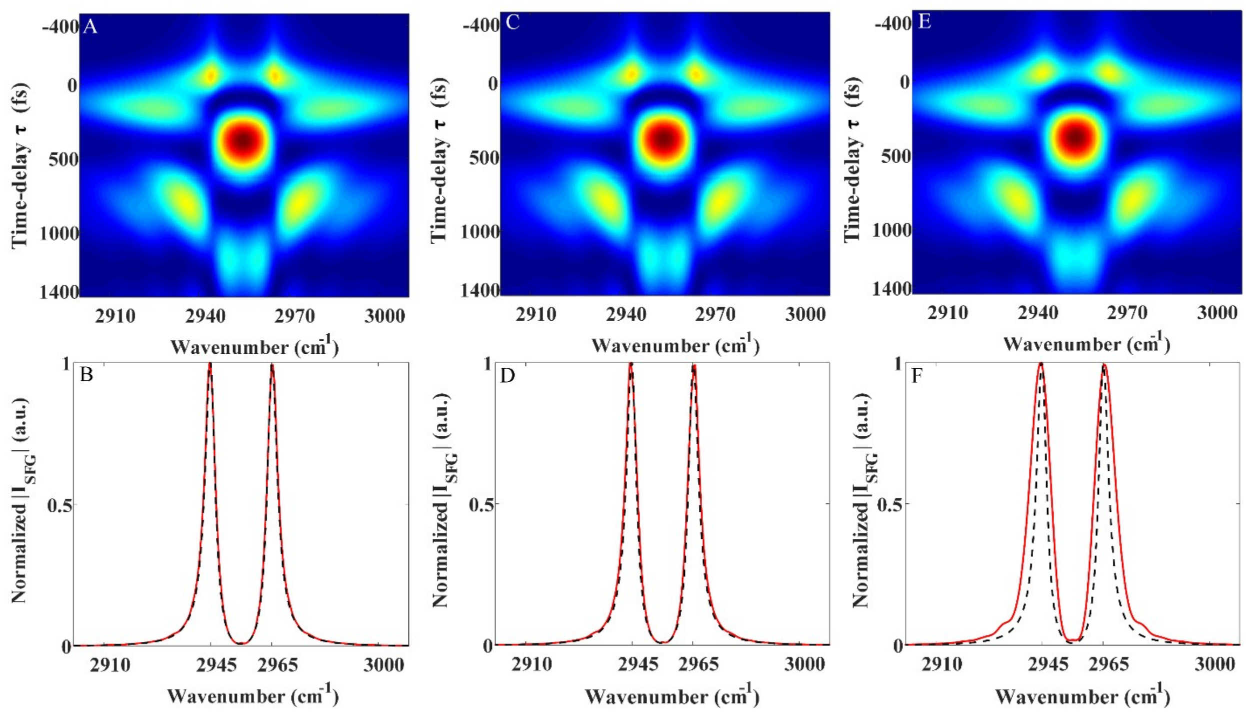

Figure S2. (A, C and E) The II-SFG spectral maps recorded by the spectrometer with resolution 0.5 cm^{-1}, 2 cm^{-1} and 5 cm^{-1}, respectively. (B, D and E) The retrieved $|P^{(1)}(\omega_{IR})|^2$ from A, C and E, respectively. The red curves are the retrieved results and the black dotted curves are the original.

4. Additional simulations based on Table 1.

4.1. The parameters of the input pulses used in Figure 2:

1) The amplitude, central frequency and temporal linewidth of the incident IR pulse are 1, 2955 cm^{-1}, and 100 fs, respectively.
2) The amplitude, central frequency and temporal linewidth of the original incident visible pulse are 1, 12500 cm^{-1}, and 100 fs, respectively.
3) The range of time-delay τ between IR and visible pulse in Figure 2(A) is from -480 fs to 1440 fs with 10 fs step.

4.2. The retrieving result without π-step phase modulation.

The spectrally- and time-resolved sum frequency generation (STiR-SFG) method[5] uses the original visible pulse without phase-modulation. As shown in Figure S3A, the STiR-SFG spectral map does not show any significant frequency characteristics. The retrieved visible pulse and the intensity of the first-order polarization are not precisely recovered, even without any noise.

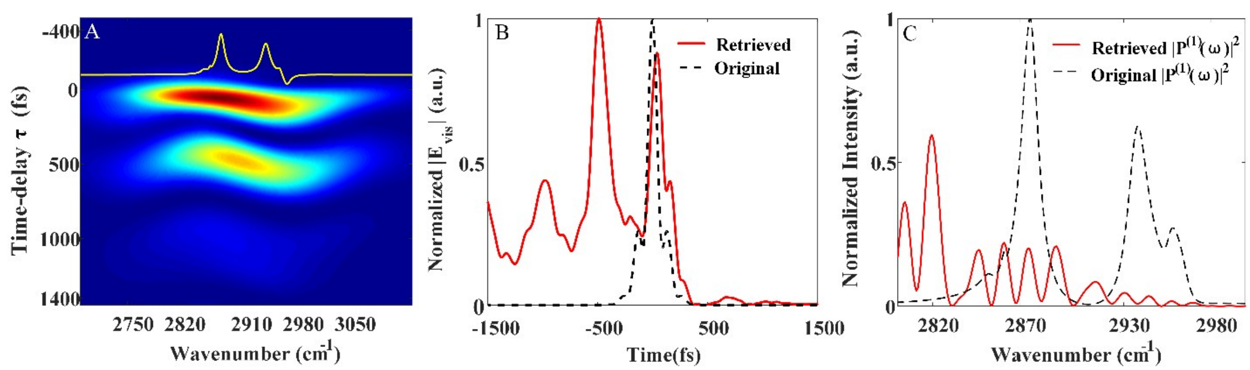

Figure S3. (A) The STiR-SFG spectral map. The yellow curve in the map is the imaginary part of the $\chi^{(2)}(\omega)$. (B) The retrieved and original visible pulse. (C) The retrieved and original intensity of frequency-domain first-order polarization.

4.3. The retrieving result of the 800 nm pulse with chirping effect.

The 800 nm pulse with a linear chirp can be expressed as,[6-7]

$$E_C(t) = A_0\left[\frac{\Delta_c^2\pi}{ln2(1+C^2)}\right]^{1/4} exp\left[-\frac{(1+iC)\Delta_c^2\pi^2t^2}{2ln2(1+C^2)}\right] exp(-i\omega_0 t)$$

where A_0 is the amplitude, ω_0 is the central frequency, Δ_c is the FWHM spectral widths of the 800 nm pulse. C is the chirp parameter defined as

$$C = \alpha\sqrt{\frac{T^2}{T_0^2} - 1},$$

where α is an constant, T_0 is the FWHM temporal width of the 800 nm pulse, related to the Δ_c by $T_0 = 2ln2/(\pi\Delta_c)$. T is the FWHM widths for the chirped pulse.

Figure S4A and B show the phase-modulated 800 nm pulse with a positive or a negative chirp, respectively.

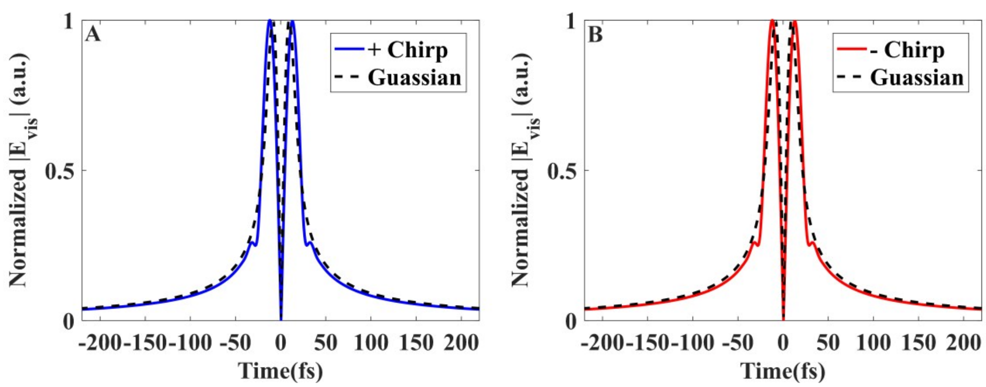

Figure S4. (A) The profile of the Gaussian 800 nm pulse (black dashed curve) and the 800 nm pulse with a positive chirp(blue) (A) and a negative chirp (red) (B).

In Figure S5, although the chirping effect significantly distorts the SFG spectra (Figure S5 A, D, and G), our approach can retrieve the distorted pulse profiles (Figure S5 B, E, and H). The spectra of the first-order polarization (Figure S5 C, F, and I) obtained using our retrieval algorithm are very similar in the presence of a chirp. Therefore, the chirping effect has been mostly removed in our retrieval algorithm.

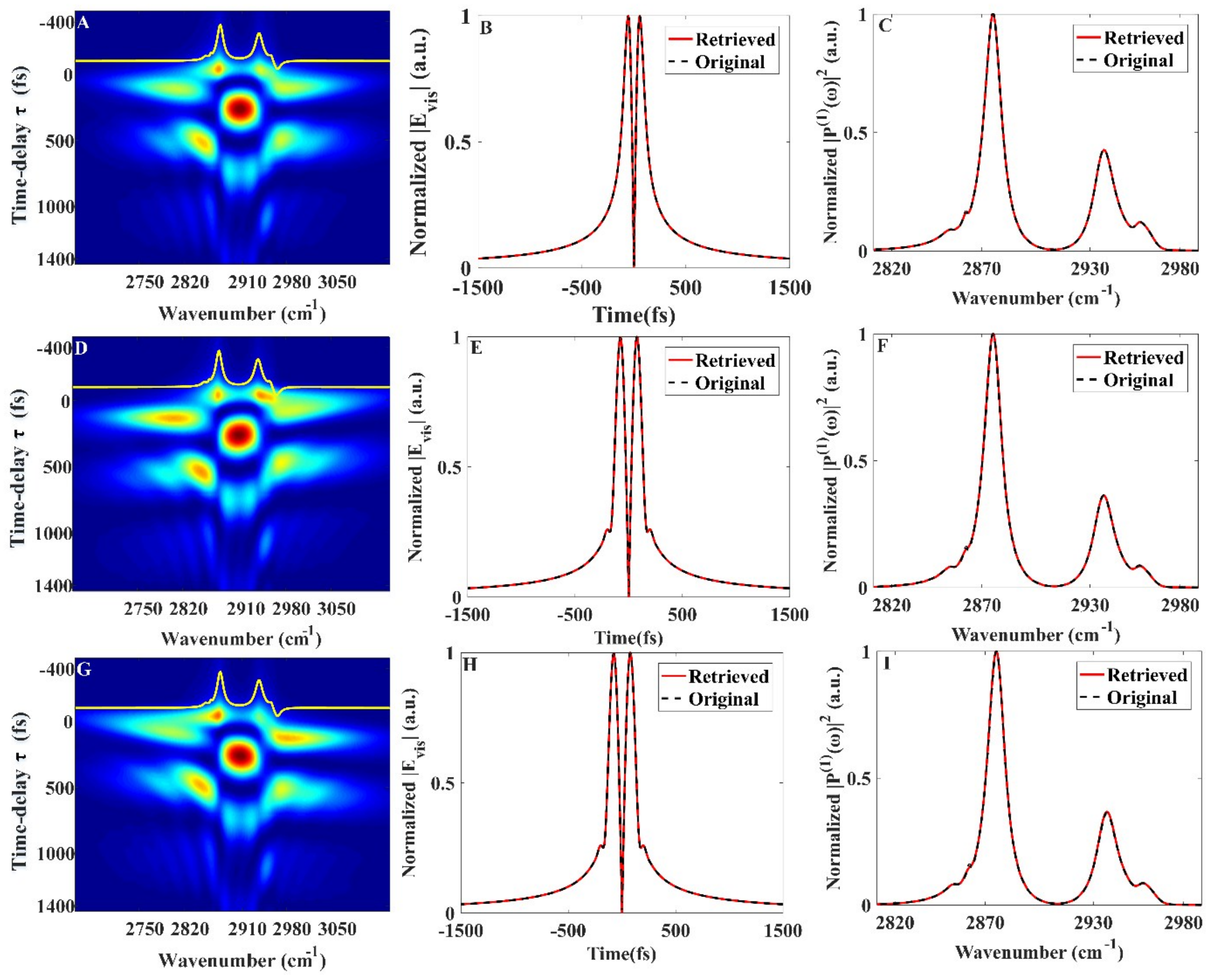

Figure S5. (A) The II-SFG spectral map with no chirp in the 800 nm pulse. (B) The retrieved 800 nm pulse from A and the original 800 nm pulse in time-domain. (C) The retrieved $|P^{(1)}(\omega_{IR})|^2$ from A and the original $|P^{(1)}(\omega_{IR})|^2$. (D) The II-SFG spectral map with a positive chirp in the 800 nm pulse. (E) The retrieved 800 nm pulse from D and the original 800 nm pulse in time-domain. (F) The retrieved $|P^{(1)}(\omega_{IR})|^2$ from D and the original $|P^{(1)}(\omega_{IR})|^2$. (G) The II-SFG spectral map with a negative chirp in the 800 nm pulse. (H) The retrieved 800 nm pulse from G and the original 800 nm pulse in time-domain. (I) The retrieved $|P^{(1)}(\omega_{IR})|^2$ from G and the original $|P^{(1)}(\omega_{IR})|^2$.

5. Additional simulations based on Table 2.

5.1. The parameters of the input pulses used in Figure 3.

1) The amplitude, central frequency and temporal linewidth of the incident IR pulse are 1, 2910 cm^{-1}, and 100 fs, respectively.
2) The amplitude, central frequency and temporal linewidth of the incident original visible pulse are 1, 12500 cm^{-1}, and 100 fs, respectively.
3) The time-delay τ of the 5 spectra labelled by the red bars in Figure 3(A) are: -50 fs, 200 fs, 450 fs, 700 fs, and 950 fs, respectively.

5.2. The optimal number of the spectra used for retrieving.

We validate the changes of the root-mean-square deviation (RMSE) between the retrieved and original second-order nonlinear susceptibility as the number of the spectra used for retrieving increasing. As shown in Figure S6, the retrieving RMSE with 5 spectra or more have a similar value. Therefore, retrieving with 5 SFG spectra is a good choice.

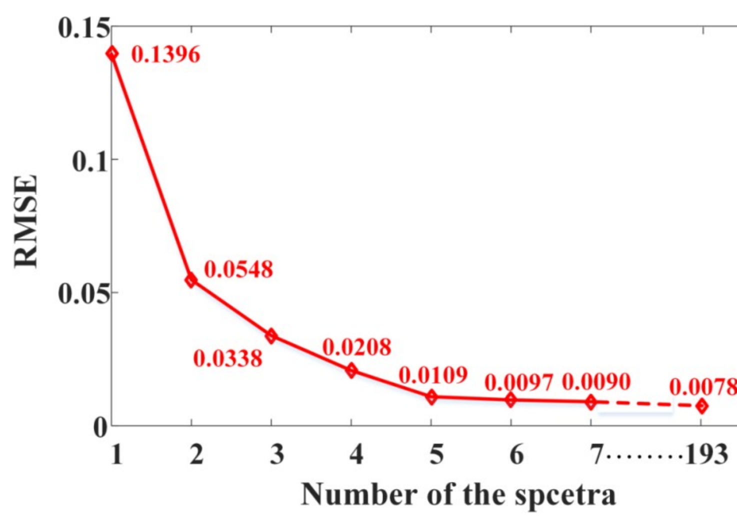

Figure S6. RMSE values between the retrieved and original second-order nonlinear susceptibility as a function of the number of the SFG spectra used for retrieving.

6. The simulated II-SFG maps of biomolecules

Figure S7A shows the simulated II-SFG map of the refolded amphiphilic peptide, LK7β. The parameters of the second-order nonlinear susceptibility are given in Table S2, which referred from Yan group's work[8]. The central frequency of the incident IR pulse is 2918 cm^{-1}. As shown in Figure S7B, the imaginary part of $\chi^{(2)}(\omega)$ can be recovered with seven vibrational peaks which have the exact vibrational frequency.

Table S2. The values of the spectral peak position, widths and amplitudes represent the spectral features of the refolded amphiphilic peptide, $LK_7\beta$ at the air−water interface.

mode	ω (cm^{-1})	Γ (cm^{-1})	A
1	2851.1	19.5	0.90
2	2868.0	22.8	0.80
3	2893.0	10.1	0.27
4	2909.0	10.3	0.70
5	2934.5	5.1	-0.63
6	2959.0	7.0	1.42
7	2984.3	10.4	0.93
		0.00084	

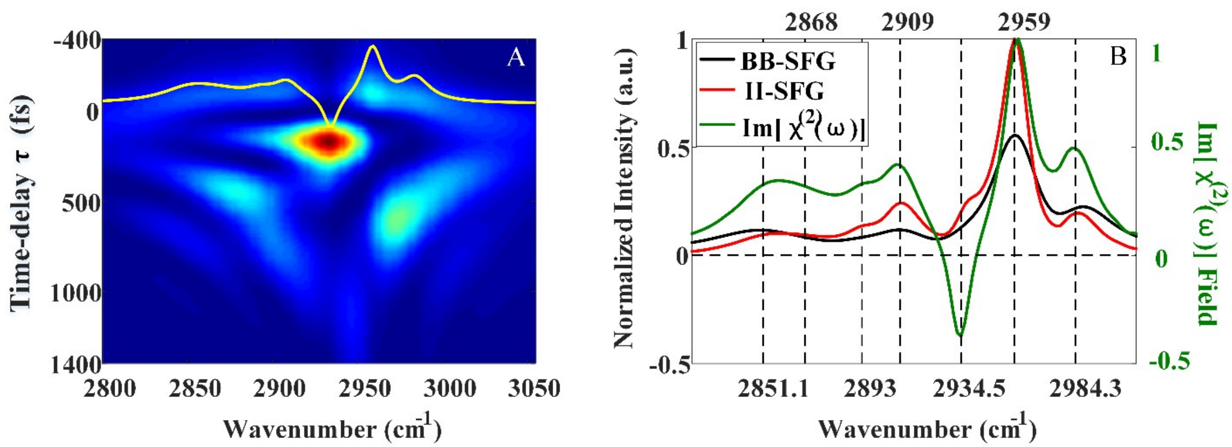

Figure S7. (A) The II-SFG spectral map of LK7β. The yellow curve in the map is the imaginary part of the $\chi^{(2)}(\omega)$. (B) The retrieved $|P^{(1)}(\omega_{IR})|^2$ (red line) and the imaginary part of the $\chi^{(2)}(\omega)$ (green line) from the II-SFG method and the I_{SFG} from BB-SFG (black line).

Figure S8A shows the simulated II-SFG map of the lactoferricin B adsorbed at aqueous–liquid crystal interfaces. The parameters of the second-order nonlinear susceptibility are given in Table S3, which referred from Chen's work[9]. The central frequency of the incident IR pulse is 1632 cm^{-1}. As shown in Figure S8B, the spectrum obtained by the II-SFG method has higher spectral resolution than that of the traditional BB-SFG spectrum.

Table S3. The values of the spectral peak position, widths and amplitudes represent the spectral features of the lactoferricin B adsorbed at aqueous–liquid crystal interfaces.

mode	ω (cm^{-1})	Γ (cm^{-1})	A
1	1600	7	8
2	1635	16	7
3	1663	23	18
A_{NR}		-0.29	

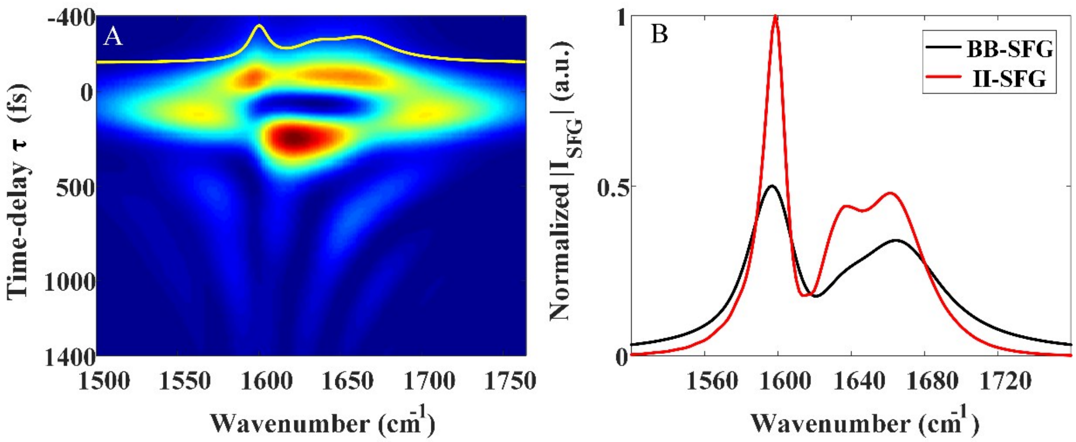

Figure S8. (A) The II-SFG spectral map of the lactoferricin B. The yellow curve in the map is the imaginary part of the $\chi^{(2)}(\omega)$. (B) The comparison of the retrieved $|P^{(1)}(\omega_{IR})|^2$ (red line) from II-SFG and the I_{SFG} from BB-SFG (black line).

7. The retrieving of the IR beam profile.

When both a higher resolution and the relative phase are needed, measurement of the IR beam profile is needed. We can record the IR-visible SFG-FROG cross correlation map (Figure S9A) while the II-SFG map (Figure S9B) is acquiring. FROG is a well-documented technique for measuring the spectral phase of short laser pulses.[10, 11] The profile of the IR pulse can be retrieved from the SFG-FROG map. With the profile of the IR pulse, we can further retrieve the $\chi^{(2)}(\omega)$ and $\chi^{(2)}(t)$. The parameters of the input pulses in this simulation are listed in section 4. The parameters of the $\chi^{(2)}$ is listed in Table 2.

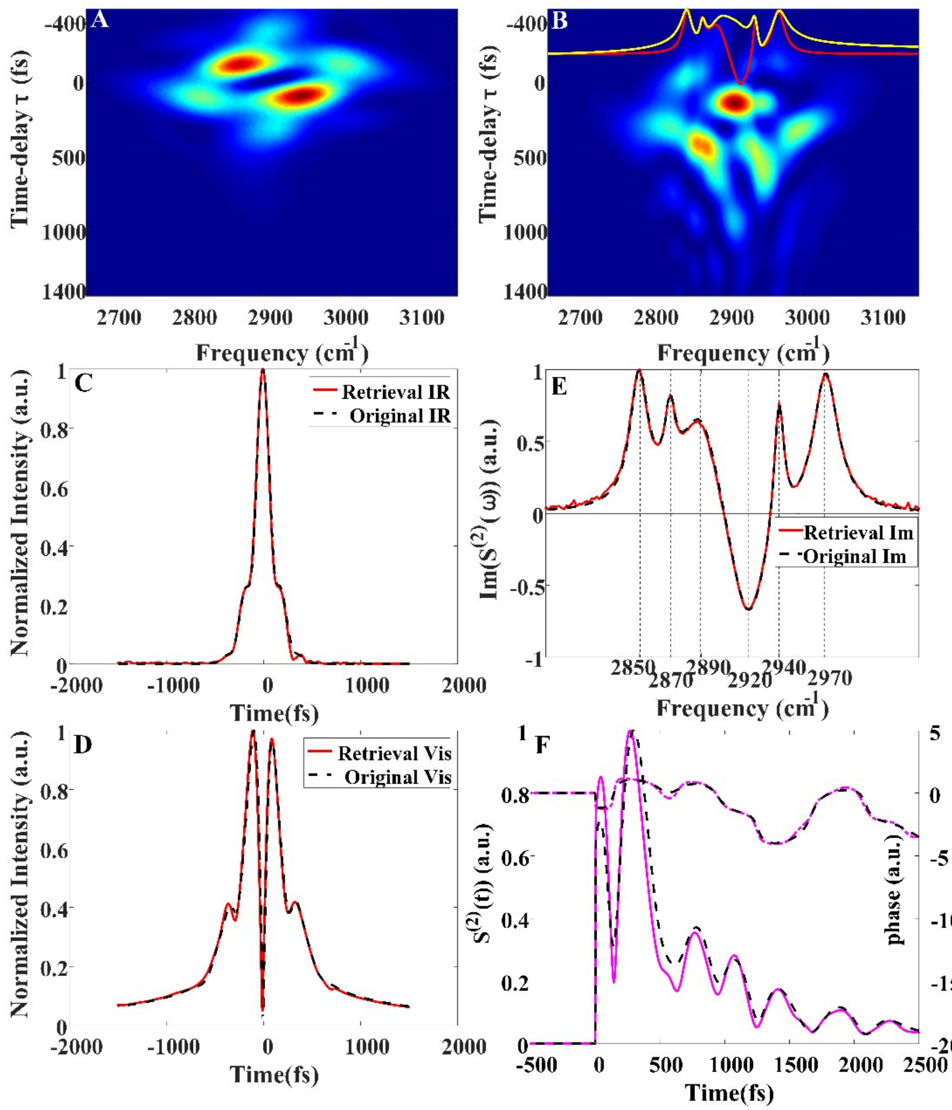

Figure S9. (A) SFG-FROG cross correlation map of the chirped IR (black dotted line in C) and π-step phase-modulated 800 nm pulse (black dotted lines D) with Poisson noise. (B) II-SFG spectral map with Poisson noise. The red and yellow lines are the imaginary part and intensity part of the $\chi^{(2)}(\omega)$, respectively. (C) and (D) Retrieved IR and 800 nm pulse (red solid lines in C and D, respectively). (E) Imaginary parts of retrieved (the red solid line) and original (the black dotted line) $\chi^{(2)}(\omega)$. (F) Intensity and phase of the retrieved (magenta solid line) and original (black solid line) $\chi^{(2)}(t)$.

8. The simulated II-SFG spectral map with and without non-resonant background

Figure S10 shows the simulated II-SFG spectral map with and without non-resonant background. The parameters of the spectral peak positions and widths of the $\chi^{(2)}(\omega)$ are listed in Table S4. The central frequency of the incident IR pulse is 3590 cm^{-1}. In Figure S10A and S10C, the amplitudes of the spectral peaks are 1, -1 and -1, respectively. In Figure S10B and S10D, the amplitudes of the spectral peaks are -1, 1 and 1, respectively. Notably, the respective imaginary parts of these two $\chi^{(2)}(\omega)$ shown as the yellow curves are totally opposite. In Figure S10A and S10B, the non-resonant background NA is 0.1. In Figure S10C and S10D, the non-resonant background is 0.

As shown in Figure S10A and S10B, the II-SFG spectral maps with the non-resonant background exhibit totally different intensity distributions varied with the $\chi^{(2)}(\omega)$. In Contrast, as shown in Figure S10C and S10D, the II-SFG spectral maps without the non-resonant background show the identical intensity patterns. The relative phases of the $\chi^{(2)}(\omega)$ can be retrieved from Figure S10A and S10B using the non-resonant background as the reference.

The non-resonant background is existent in most of the $\chi^{(2)}(\omega)$. For the exceptional case which the non-resonant background is absent, the SFG signal of the gold or crystal substrate can be adopted as the reference.

Table S4. The values of the spectral peak positions and widths

mode	ω (cm^{-1})	Γ (cm^{-1})
1	3550	2
2	3590	2
3	3630	2

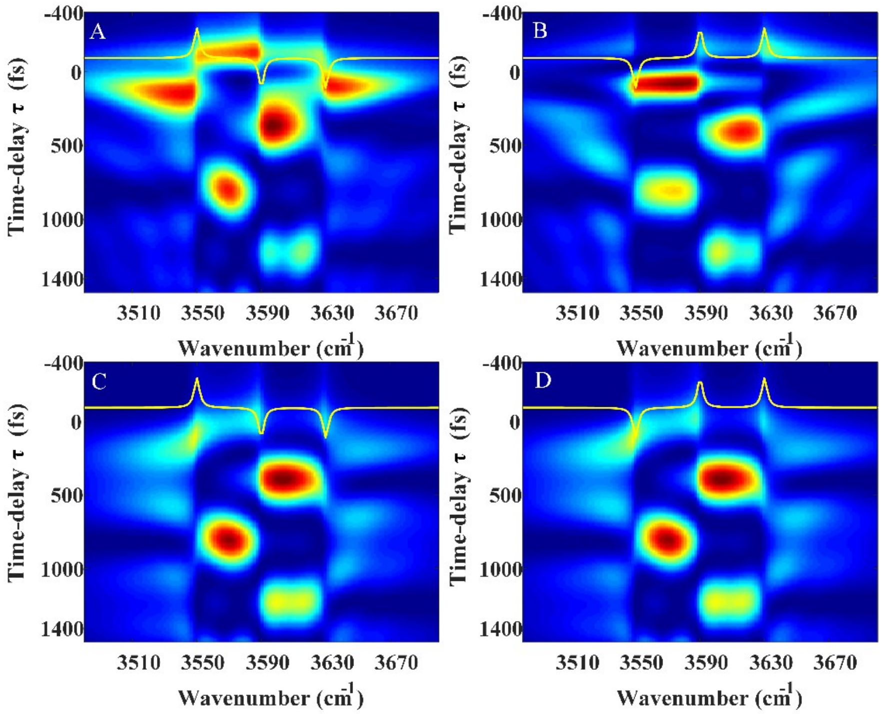

Figure S10. (A) and (B) The II-SFG spectral maps with the non-resonant background. (C) and (D) The II-SFG spectral maps without the non-resonant background. The yellow curves in the maps are the respective imaginary part of the $\chi^{(2)}(\omega)$.

9. References

(1) Mukamel, S.; Mukamel, S. *Principles of nonlinear optical spectroscopy*. Oxford University Press, New York, USA, 1995.

(2) Bordenyuk, A. N.; Jayathilake, H.; Benderskii, A. V. Coherent vibrational quantum beats as a probe of Langmuir-Blodgett monolayers. *J. Phy. Chem. B.* **2005**, *109*, 15941-15949.

(3) Nihonyanagi, S.; Eftekhari-Bafrooei, A.; Borguet, E. Ultrafast vibrational dynamics and spectroscopy of a siloxane self-assembled monolayer. *J. Chem. Phys.* **2011**, *134*, 084701.

(4) Roke, S.; Bonn, M.; Petukhov, A. V. Nonlinear optical scattering: The concept of effective susceptibility. *Phys. Rev. B.* **2004**, *70*, 2516-2528.

(5) Bordenyuk, A. N.; Benderskii, A. V. Spectrally- and time-resolved vibrational surface spectroscopy: Ultrafast hydrogen-bonding dynamics at D(2)O/CaF(2) interface. *J. Chem. Phys.* **2005**, *122,* 134713.

(6) Knutsen, K. P.; Messer, B. M.; Onorato, R. M.; Saykally, R. J. Chirped coherent anti-stokes Raman scattering for high spectral resolution spectroscopy and chemically selective imaging. *J. Phys. Chem. B.* **2006**, *110*, 5854-64.

(7) Pegoraro, A. F.; Ridsdale, A.; Moffatt, D. J.; Jia, Y.; Pezacki, J. P.; Stolow, A. Optimally chirped multimodal CARS microscopy based on a single Ti:sapphire oscillator. *Opt. Express.* **2009**, *17*, 2984.

(8) Wang, Z.; Fu, L.; Yan E. C. C−H Stretch for Probing Kinetics of Self-Assembly into Macromolecular Chiral Structures at Interfaces by Chiral Sum Frequency Generation Spectroscopy. *Langmuir.* **2013**, 29, 4077-4083.

(9) Wang, X.; Yang, P.; Mondiot, F.; Li, Y.; Miller, D. S.; Chen, Z.; Abbott N.L. Interfacial ordering of thermotropic liquid crystals triggered by the secondary structures of oligopeptides. *Chem. Commun.* **2015**, 51, 16844-16847.

(10) Kane D.J.; Trebino R. Using phase retrieval to measure the intensity and phase of ultrashort pulses: frequency-resolved optical gating. *J. Opt. Soc. Am. A*. **1993**, 10, 1101-1111.

(11) Kohler B.; Yakovlev V.V.; Wilson K.R.; Squier J.; Delong K.W.; Trebino R. Phase and intensity characterization of femtosecond pulses from a chirped-pulse amplifier by frequency-resolved optical gating. *Opt. Lett.* **1995**, 20, 483-485.